Stability and accuracy of finite element direct solvers for Electrical Impedance Tomography

Thierry Martin and Jérôme Idier

Abstract

Electrical impedance tomography (EIT) of closed conductive media is an ill-posed inverse problem. In the general case, the resolution of the direct problem, derived from a second order partial derivative equation, requires a numerical approximation. The solution brought by the Finite Element Method (FEM) is often used in EIT, because it preserves the nonlinear dependence of the observation set upon the conductivity distribution.

This paper addresses the reliability of numerical FEM direct solvers, as basic tools in 2D EIT inversion methods. Reliability is closely related to the *discretization error* of the FEM model but also to its *numerical stability*. Finely discretized FEM models yield reduced discretization errors. Meanwhile, special attention must be paid to stability since a more accurate FEM direct model involves a magnification of input *round-off errors*. A theorem is established that allows easy checking of the numerical stability through the computation of the condition number of the *uniform stiffness matrix* of the FEM solver. When the latter is stable, global inaccuracy reduces to the *discretization error* of the FEM approximation. Simulations reveal that, provided input current patterns are spatially smooth, the variations of the conductivity distribution have a limited but non negligeable influence on the discretization error.

Keywords

T. Martin and J. Idier are with the Laboratoire des Signaux et Systèmes (CNRS–Suplec–UPS), Suplec, Plateau de Moulon, 91192 Gif-sur-Yvette cedex, France (email: martin@lss.supelec.fr and idier@lss.supelec.fr)

Electrical Impedance Tomography, Finite Element Methods, Numerical stability, Discretization errors

I. Introduction

Electrical Impedance Tomography (EIT) of closed conductive media with steady currents is a non-invasive imaging technique. It aims at estimating the impedance distribution within a conductive body from electrical measurements on the surface. Usually, thanks to surface electrodes, the experiment consists in injecting currents in the body and measuring the surface voltage distributions. Numerical estimation methods, closely related to well-known Algebraic Reconstruction Techniques (ART), have been early used to solve this inverse problem ([1], [2], [3]). Such computed imaging methods require (either explicitly or implicitly) a numerical direct model $\boldsymbol{z} = h(\boldsymbol{x})$ (where $\boldsymbol{x}$ stands for the sought object and $\boldsymbol{z}$ contains the observed data).

The aim of the present paper is to show that direct models provided by the Finite Element Method (FEM) are *accurate* enough (w.r.t. the theoretical analytical model) but also *numerically stable* enough to use in EIT inversion methods. This is not a straightforward issue because the FEM direct model is a *nonlinear* solver. For EIT and for other problems deriving from *partial derivative equations* (PDE), the choice of a linear direct model (such as Born or Rytov approximations) is accurate only in restricted conditions (limited width or magnitude of inhomogeneities). For the last two decades, nonlinear (w.r.t. $\boldsymbol{x}$) numerical models derived from FEM, or Finite Difference Methods (FDM) have been more and more used because they provide a better accuracy. Such models read

$$\boldsymbol{z} = f([\boldsymbol{A}(\boldsymbol{x})]^{-1})\boldsymbol{y}, \tag{1}$$

where $\boldsymbol{y}$ and $\boldsymbol{z}$ concatenate the observed measures and $\boldsymbol{A}(\boldsymbol{x})$ is an invertible operator which linearly depends upon $\boldsymbol{x}$. Higher computation capacity favors good accuracy, thanks to a larger number of points in $\boldsymbol{y}$, but at the expense of increased instabilities linked to the condition number of the matrix $\boldsymbol{A}(\boldsymbol{x})$.

Studying the accuracy of the direct problem meets with three difficulties, identified in [4] as three kinds of inaccuracy or *errors* appearing in the construction of the direct solver:

- The *mathematical modeling error* corresponds to the difference between the actual physical behavior and the mathematical model. In EIT, the mathematical model is the (rarely explicit) solution of an elliptic second order PDE derived from Maxwell equations. Apart from technical or geometrical simplifying hypotheses, the mathematical error also incorporates 2D and steady current approximations (low-frequency currents are actually used in most EIT experiments). Characterizing such approximations is out of the scope of the present paper.
- The *discretization error* is the theoretical distance between the exact solution of the mathematical model and the algebraic model (1). In this paper, a FEM algebraic model is chosen. Actually, FEM provides a piecewise polynomial approximation that can be identified from values on a limited number of points (stacked in vectors $\boldsymbol{x}$, $\boldsymbol{y}$ and $\boldsymbol{z}$). The discretization error is thus the distance between the piecewise polynomial approximation and the theoretical solution of the PDE. The difficulty consists in estimating this distance in order to provide a direct model that is accurate enough to solve the EIT inverse problem.
- *Round-off errors* correspond to the loss of accuracy due to the limitations of computing machines. Here, eq. (1) involves a matrix inversion for the direct model so that one may expect an important magnification of *round-off* errors through the direct (numerical) model. As a result, contrary to linear (implicitly well-posed) direct models, the question of numerical stability arises for such a nonlinear direct model. In the litterature, this question is tackled only w.r.t. the observed vector $\boldsymbol{y}$ [5], with the analysis of the condition number of the matrix $\boldsymbol{A}(\boldsymbol{x})$. Here, in order to solve the inverse problem, this question is also addressed w.r.t. the unknown object $\boldsymbol{x}$. Actually, it is important that the round-off error be small enough to preserve the accuracy of the direct model but also that this error be *negligible* (w.r.t. the output), so that the numerical direct model can be identified with the algebraic direct model. The issue at stake is the possibility to tackle the inverse problem resolution in the classical algebraic sense, as done for instance in [6], [7], [8] with a Bayesian approach.

The article is organized as follows:

- In Section II, the FEM EIT direct model is given. For the sake of clarity in the next

sections, specific EIT notations are adopted.

- In Section III, special care is paid to the question of stability of the direct model and to the evaluation of the resulting *round-off errors*. A theorem is established, yielding an upper bound for the uncertainties on the output $\boldsymbol{z}$ w.r.t. input uncertainties on $\boldsymbol{y}$ and $\boldsymbol{x}$, as a function of the condition number of $\boldsymbol{A}(\boldsymbol{x} = \mathbf{1})$, *i.e.,* of $\boldsymbol{A}$ where the sought object is uniform. Then, we provide typical extreme eigenvalues of $\boldsymbol{A}(\boldsymbol{x} = \mathbf{1})$ for some *concentric layer circular meshes* (CLCM) frequently used in 2D FEM domain triangulation, and for two other kinds of triangularized domains. We show that the direct model computation involves a magnification of the input round-off errors by several orders of magnitude. However, FEM solvers studied in this paper and used in inversion methods in [6], [7], [8] are coded on a sufficiently large number of digits to preserve the negligibility of the output round-off error w.r.t. the output voltage magnitude.
- In Section IV, a more qualitative study is conducted concerning the *discretization error*. In a case where there exists an explicit solution to the EIT PDE, we show that the discretization accuracy is more sensitive to the choice of the input current pattern than to the choice of the conductivity distribution. Then, we take advantage of the existence of a *dual* direct model in 2D to provide a rough but cheap estimator of the discretization error. From this we can see that, provided the input current pattern is correctly chosen (*i.e.,* as a spatially smooth varying distribution), the final precision of typical direct models (used in [6], [7], [8]) approximately ranges from 45 to 70 dB, which happens to be satisfactory to solve the inverse problem.

II. FEM direct model for EIT

In EIT, the image-data relation derived from Maxwell formulas is ruled by a second order PDE which yields no analytical solution for arbitrary domain shapes or arbitrary conductivity distributions. Therefore, one has to approximate the direct problem. Since the mid 80's, the Finite Element Method (FEM) has been more often used to solve it [9], [10], [11], [12], [6]. In this section, the goal is to give a synthetic presentation of the algebraic direct model. The adopted notations might slightly differ from usual FEM notations, because they are especially chosen to match with algebraic notations used in

the terminology of inverse problems. More details about the direct model can be found in general publications on FEM such as [13], [4], or in [6] where its construction is given in details.

Let Ω denote a 2D domain and $\bar{\Omega}$ its boundary. Let V and I be respectively the voltage and current distribution on Ω and $\bar{V}$ and $\bar{I}$ their restriction on $\bar{\Omega}$. Finally, $\vec{j}$ and $\vec{E}$ are the current density and the electrical field. From Maxwell formula $\vec{\nabla} \times \vec{E} = 0$, we deduce the existence of the voltage potential according to

$$\vec{E} = -\vec{\nabla} V \tag{2}$$

and from the formula $\nabla \vec{j} = 0$ we also deduce the existence (for 2D modelization only) of the current stream potential

$$\vec{j} = (\vec{\nabla} I)^{\perp}, \tag{3}$$

where $(x, y)^{\perp} = (-y, x)$ stands for the counterclockwise 90° rotation of the 2D vector (x, y). Thanks to eq. (3), the *variational* expression of the problem can be formulated according to

$$\Pi(V, I, \sigma) = \frac{1}{2} \iint_{\Omega} \left[\sigma |\vec{\nabla} V|^2 \ + \sigma^{-1} |\vec{\nabla} I|^2 \right] \, dx \, dy + \oint_{\bar{\Omega}} \bar{V} \frac{\partial \bar{I}}{\partial s} \, ds. \tag{4}$$

Then, the FEM consists in solving a discretized form of the equation $\Pi(V, I, \sigma) = 0$. In the FEM model adopted here, Ω is discretized into a triangularized domain Ω_h composed of P adjacent triangular elements. The latter define N nodes and $\bar{N}$ boundary nodes ($\bar{N} < N < P$). The standard choice for FEM in EIT provides an approximation of σ that is piecewise constant on each element and approximations of V and I that are piecewise linear on each element of Ω_h. Let us denote respectively $\boldsymbol{v}$ and $\boldsymbol{i}$ the voltage and current stream vectors (of length N) defined by the resulting approximate distribution values of V and I on every node of the mesh and $\boldsymbol{\sigma}$ (of length P) the vector containing conductivity values ($\sigma_p > 0, \ p = 1, .., P$) defined on each element. Then, the direct EIT model reads [13]:

$$\boldsymbol{v} = \boldsymbol{A}_{\boldsymbol{\sigma}}^{-1} \bar{\boldsymbol{P}}^{\mathrm{t}} \boldsymbol{D} \bar{\boldsymbol{i}}. \tag{5}$$

Its restriction on the boundary, which is the observable part of the vector, reads

$$\bar{\boldsymbol{v}} = \bar{\boldsymbol{P}} \boldsymbol{A}_{\boldsymbol{\sigma}}^{-1} \bar{\boldsymbol{P}}^{\mathrm{t}} \boldsymbol{D} \bar{\boldsymbol{\imath}}, \tag{6}$$

where $\bar{\boldsymbol{v}} := \bar{\boldsymbol{P}} \boldsymbol{v}$ and $\bar{\boldsymbol{\imath}} := \bar{\boldsymbol{P}} \boldsymbol{i}$ are respectively the (observed) restriction of $\boldsymbol{i}$ and $\boldsymbol{v}$ on the boundary. Matrix $\bar{\boldsymbol{P}}$ $(\bar{N} \times N)$ is merely a binary matrix that operates the projection on the boundary $\bar{\Omega}$. $\boldsymbol{D}$ $(\bar{N} \times \bar{N})$ is the first order boundary difference matrix defined by

$$\boldsymbol{D}_{ij} := \begin{cases} 1/2 & \text{if } j = i - 1 \bmod \bar{N}, \\ -1/2 & \text{if } j = i + 1 \bmod \bar{N}, \\ 0 & \text{otherwise ;} \end{cases} \tag{7}$$

Lastly, $\boldsymbol{A}_{\boldsymbol{\sigma}}$ $(N \times N)$ is the *stiffness matrix* of the problem. It is very sparse (less than $7N$ of its entries are nonzero) and depends linearly upon σ. In [7], it is shown that this matrix can read:

$$\boldsymbol{A}_{\boldsymbol{\sigma}} = \boldsymbol{Q}^{\mathrm{t}} \boldsymbol{\Delta}_{\boldsymbol{\sigma}} \boldsymbol{Q}, \tag{8}$$

where $\boldsymbol{\Delta}_{\boldsymbol{\sigma}}$ $(4P \times 4P)$ is a diagonal matrix defined by

$$\boldsymbol{\Delta}_{\boldsymbol{\sigma}} = \mathrm{diag}\,[\boldsymbol{\sigma}^{\mathrm{t}}, \boldsymbol{\sigma}^{\mathrm{t}}, \boldsymbol{\sigma}^{\mathrm{t}}, \boldsymbol{\sigma}^{\mathrm{t}}]^{\mathrm{t}}$$

and $\boldsymbol{Q}$ $(4P \times N)$ is a full rank sparse matrix, solely depending upon the geometric features of the triangular mesh. Let us mention that $\boldsymbol{Q}$ has no unit and that, because of the 2D modelization, $\bar{\boldsymbol{v}}$ is in Volt, $\bar{\boldsymbol{\imath}}$ is in $\mathrm{A.m}^{-1}$ and $\boldsymbol{\sigma}$ is in $\Omega^{-1}.\mathrm{m}^{-1}$. Let us introduce the *uniform stiffness matrix* (USM) $\boldsymbol{\Theta} := \boldsymbol{Q}^{\mathrm{t}} \boldsymbol{Q}$, which is a particular case of $\boldsymbol{A}_{\boldsymbol{\sigma}}$ when $\boldsymbol{\sigma} = \boldsymbol{1}$ and plays a central role in the next section.

Remark II.1 (Implementation and computational cost of the direct model)

The direct model is implemented on *Matlab*® software, which provides specific tools to handle sparse arrays. Taking the sparsity of $\boldsymbol{A}_{\boldsymbol{\sigma}}$ into account allows to decrease the computational cost of the linear system (5) drastically [11], [14]. To evaluate the effective cost as a function of the number of nodes, let us consider direct models built on circular domains with *concentric layer circular meshes* (CLCM) (*cf.* Fig. 1). Such a family of

meshes reveals quite adapted to triangulate circular domains frequently used in EIT (for instance, [9]). CLCM use the geometric properties of the circle to build meshes iteratively by adding a new concentric layer of elements according to the following rule: if l is the number of the current layer (layers are numbered from the center), $8l + 4$ triangular elements (*i.e.,* $4l$ nodes) are required to generate the $(l + 1)$th layer of the mesh (*cf.* Fig. 1). If N_l, N and P are respectively the total number of layers, nodes and elements, we find

$$\begin{cases} N = 1 + 2N_l(N_l + 1), \\ P = 4N_l^2. \end{cases} \tag{9}$$

The computational cost reveals particularly low since it is below the equivalent cost of a linear approximation (product of a full matrix $(N \times N)$ by a vector, *cf.* Fig 2). The cost of the resolution for a full linear system is known to be $O(N^3)$ floating point operations [14]. Since in our case the number of nonzero points in $\boldsymbol{A}_{\boldsymbol{\sigma}}$ is below $7N$, a cost of about $O(N^2)$ can be reached thanks to iterative algorithms such as Gauss-Seidel Methods.

III. Round-off error

Input quantities $\bar{\boldsymbol{\imath}}$ and $\boldsymbol{\sigma}$ are real valued vectors. Thus, their storage on computing machines implies a possible round-off error caused by truncation of low-weight bits of their binary coding. Hence, the use of the direct model (6) may involve magnifications of this discrepancy, yielding possibly erroneous output results. In this section, a theorem is established to evaluate this magnification when the algebraic model is considered in its unrestricted sense (*i.e.,* $\boldsymbol{v} = \boldsymbol{A}_{\boldsymbol{\sigma}}^{-1}\bar{\boldsymbol{P}}^{\mathrm{t}}\boldsymbol{D}\bar{\boldsymbol{\imath}}$). For the sake of simplicity, the quantity $\boldsymbol{j} := \bar{\boldsymbol{P}}^{\mathrm{t}}\boldsymbol{D}\bar{\boldsymbol{\imath}}$ is involved in the theorem instead of $\bar{\boldsymbol{\imath}}$. Vector $\boldsymbol{j}$ can be interpreted as a *global* and *differential* input current distribution ($\boldsymbol{j}(n) = 0$ if n is not a boundary node).

A. Upper bounding of the uncertainty on the output voltage

Two possible causes of uncertainties $\delta\boldsymbol{v}$ on the output voltage are considered: conductivity uncertainties $\delta\boldsymbol{\sigma}$ and current uncertainties $\delta\boldsymbol{j}$, so that the output voltage becomes:

$$\boldsymbol{v} + \delta\boldsymbol{v} = \boldsymbol{A}_{\boldsymbol{\sigma}+\delta\boldsymbol{\sigma}}^{-1}(\boldsymbol{j} + \delta\boldsymbol{j}). \tag{10}$$

Let

$$\begin{aligned} |\delta\boldsymbol{\sigma}|_{\max} &:= \|\delta\boldsymbol{\sigma}\|_\infty = \max_p |\delta\sigma_p|\,, \\ \boldsymbol{\sigma}_{\min} &:= \min_p \sigma_p, \\ \boldsymbol{\sigma}_{\max} &:= \max_p \sigma_p, \end{aligned}$$

and let $\lambda_{\boldsymbol{\Theta}}^{\max} := \|\boldsymbol{\Theta}\|_2$ and $\lambda_{\boldsymbol{\Theta}}^{\min} := \left\|\boldsymbol{\Theta}^{-1}\right\|_2^{-1}$ respectively denote the largest and smallest eigenvalues of the USM $\boldsymbol{\Theta} = \boldsymbol{Q}^{\mathrm{t}}\boldsymbol{Q}$.

Theorem III.1 (Upper bounding of $\|\delta\boldsymbol{v}\|_2 / \|\boldsymbol{v}\|_2$)

If the condition

$$\frac{|\delta\boldsymbol{\sigma}|_{\max}}{\boldsymbol{\sigma}_{\min}} < \frac{\lambda_{\boldsymbol{\Theta}}^{\min}}{\lambda_{\boldsymbol{\Theta}}^{\max}} \tag{11}$$

holds, then the norm of the output uncertainty $\delta\boldsymbol{v}$ defined in eq. (10), is upper bounded w.r.t. $\|\boldsymbol{v}\|_2$ by

$$\frac{\|\delta\boldsymbol{v}\|_2}{\|\boldsymbol{v}\|_2} \leqslant \frac{\boldsymbol{\sigma}_{\max}(\lambda_{\boldsymbol{\Theta}}^{\max})^2\,|\delta\boldsymbol{\sigma}|_{\max}}{\boldsymbol{\sigma}_{\min}\lambda_{\boldsymbol{\Theta}}^{\min}(\boldsymbol{\sigma}_{\min}\lambda_{\boldsymbol{\Theta}}^{\min} - |\delta\boldsymbol{\sigma}|_{\max}\lambda_{\boldsymbol{\Theta}}^{\max})} + \frac{\boldsymbol{\sigma}_{\max}\lambda_{\boldsymbol{\Theta}}^{\max}\,\|\delta\boldsymbol{j}\|_2}{(\boldsymbol{\sigma}_{\min} - |\delta\boldsymbol{\sigma}|_{\max})\lambda_{\boldsymbol{\Theta}}^{\min}\,\|\boldsymbol{j}\|_2}. \tag{12}$$

The proof is given in the appendix. Note that, as far as modern computers are concerned, condition (11) is not restrictive : in the case of *standard ANSI/IEEE 64-bit coding* (commonly called *double precision*), the order of a relative quantity such as the relative conductivity discrepancy $\delta\boldsymbol{s} := \delta\boldsymbol{\sigma}/\boldsymbol{\sigma}_{\min}$ is given by the *floating point relative accuracy* $\mathtt{eps} = 2.22\,10^{-16}$ ([14]). For practical sake, a fully normalized version of this theorem can be easily derived. Let us introduce the relative current variation $\delta\boldsymbol{c} := \delta\boldsymbol{j}/\,\|\boldsymbol{j}\|_2$ and the relative voltage variation $\delta\boldsymbol{u} := \delta\boldsymbol{v}/\,\|\boldsymbol{v}\|_2$. Let us also denote $\rho_\sigma := \boldsymbol{\sigma}_{\max}/\boldsymbol{\sigma}_{\min}$ and $\kappa_{\boldsymbol{\Theta}} := \lambda_{\boldsymbol{\Theta}}^{\max}/\lambda_{\boldsymbol{\Theta}}^{\min}$ the contrast of $\boldsymbol{\sigma}$ and the condition number of $\boldsymbol{\Theta}$, respectively.

Corollary III.1: If $|\delta\boldsymbol{s}|_{\max} < \kappa_{\boldsymbol{\Theta}}^{-1}$, then

$$\|\delta\boldsymbol{u}\|_2 \leqslant \|\delta\boldsymbol{u}\|_2^{\sup} = \frac{\kappa_{\boldsymbol{\Theta}}^2\rho_\sigma}{1 - \kappa_{\boldsymbol{\Theta}}\,|\delta\boldsymbol{s}|_{\max}}\,|\delta\boldsymbol{s}|_{\max} + \frac{\rho_\sigma\kappa_{\boldsymbol{\Theta}}}{1 - |\delta\boldsymbol{s}|_{\max}}\,\|\delta\boldsymbol{c}\|_2\,. \tag{13}$$

B. Order of magnitude of the output round-off error in the computation of standard EIT FEM direct model

The number of nodes used in various contributions in the field of EIT ranges from 50 [9] to 6000 [15]. Basically, it is expected that the discretization error be reduced as the

number of mesh-nodes increases (this question is addressed in Section IV). However, the bound $\|\delta \boldsymbol{u}\|_2^{\sup}$ of eq. (13) crucially depends on the condition number $\kappa_{\boldsymbol{\Theta}}$, which might increase as the mesh gets finer.

In order to derive the order of magnitude of $\|\delta \boldsymbol{u}\|_2^{\sup}$, let us examine the value of $\kappa_{\boldsymbol{\Theta}}$ w.r.t. the number of nodes. As a general rule, the condition number of FEM stiffness matrices highly depends on the mesh quality. Especially, 2D triangular meshes bring badly conditioned USM if some of their elements are far from equilaterality [16]. Even a single distorted element is enough to make a mesh unsuited to FEM computations. On the other hand, automatic schemes, such as Delaunay triangulation, yield appropriate meshes [17]. Here, to study $\kappa_{\boldsymbol{\Theta}}$ w.r.t. N, we use again the CLCM family presented formerly, which provides no distorted element. Figure 3 shows that $\lambda_{\boldsymbol{\Theta}}^{\max}$ is quasi-constant w.r.t. N while $\lambda_{\boldsymbol{\Theta}}^{\min}$ decreases quasi-linearly in a log-log scale. The CLCM displayed on Fig. 1 ($N = 145$) was used in [18] in an EIT inversion method. For this mesh, numerical computations yield $\lambda_{\boldsymbol{\Theta}}^{\max} = 7.06$ and $\lambda_{\boldsymbol{\Theta}}^{\min} = 0.0121$. On the other hand, most conductivity distributions have a contrast not higher than $\rho_\sigma^{\max} = 100$. For such numerical values, eq. (13) reads:

$$\|\delta \bar{\boldsymbol{u}}\|_2 \leqslant \frac{3.4\ 10^7}{1 - 583\,|\delta \boldsymbol{s}|_{\max}}\,|\delta \boldsymbol{s}|_{\max} + \frac{5.83\ 10^4}{1 - |\delta \boldsymbol{s}|_{\max}}\,\|\delta \boldsymbol{c}\|_2\,,$$

if $|\delta \boldsymbol{s}|_{\max} < 1/583$. By reference to the aforementioned 64-bit coding, let us consider $|\delta \boldsymbol{s}|_{\max} = \|\delta \boldsymbol{c}\|_2 = \texttt{eps} = 2.22\ 10^{-16}$. Then, the condition $|\delta \boldsymbol{s}|_{\max} < 1/583$ is easily fulfilled and we obtain the following relative output uncertainty for the direct model:

$$\|\delta \bar{\boldsymbol{u}}\|_2 \leqslant 7.57\ 10^{-9},$$

which can be considered *negligible* w.r.t. one. If the number of nodes is 6000, extrapolation on Fig. 3 yields $\lambda_{\boldsymbol{\Theta}}^{\max} \approx 10$ and $\lambda_{\boldsymbol{\Theta}}^{\min} \approx 3\ 10^{-4}$. With the same hypothesis as above, condition (11) is also fulfilled and inequality (13) reads $\|\delta \bar{\boldsymbol{u}}\|_2 \leqslant 2.47\ 10^{-5}$. The latter bound may not be considered negligible w.r.t. one. In that case, a numerically more *stable* direct model would require to be coded on a greater number of digits.

For sake of exhaustivity, we have considered two other typical meshes: the first one is a non convex *peanut shaped* hand meshed domain, and the second one is a convex *potato shaped* domain meshed by Delaunay triangulation ([17]). In both cases, extreme USM

eigenvalues are provided for two different degrees of refinement (Fig. 8), and upper bounds are displayed in Table I under the same hypotheses as above. On these typical meshes, double-precision (64-bit) coding for the inputs (conductivity and current) yields at least a 6-digit precision for the output voltage. Such a precision can be regarded as sufficient to tackle successfully the inverse problem, as long as the latter is properly *regularized*.

As a more general matter, with the view to identifying the algebraic and the numerical FEM direct models, it must be kept in mind that magnification of input round-off errors may vary from *several* orders of magnitudes. Given Corollary III.1, computation of the USM condition number $\kappa_{\mathbf{\Theta}}$ (even roughly for larger matrices) provides an easy way to detect possible round-off problems.

IV. Discretization error

As reported in general books devoted to FEM, it is known that convergence toward the exact solution of the PDE is mathematically obtained as the size of the elements decreases. In [13], it is expressed by the following theorem:

Theorem IV.1 (EIT FEM convergence rate) Let $\bar{I}$ denote a piecewise linear current distribution, injected on the boundary $\bar{\Omega}$ of a polygonal domain Ω and let $E = V^* - \widehat{V}$ be the difference between the exact solution V^* and the FEM estimated solution $\widehat{V}$ on Ω. Let us also introduce the diameter h of the largest element in the triangularization Ω_h of Ω.

Then, there exists a positive constant C such that

$$\|E\|_2 \leqslant Ch^2 \max_{(x,y)\in\Omega} \max \left\{ \left| \frac{\partial^2 V}{\partial x^2} \right|, \left| \frac{\partial^2 V}{\partial x\, \partial y} \right|, \left| \frac{\partial^2 V}{\partial y^2} \right| \right\}, \tag{14}$$

where the norm $\|.\|_2$, is associated to the Sobolev space $H^1(\Omega) = W_2^1(\Omega)$. It is defined by:

$$\|U\|_2 = [\langle U, U\rangle + \langle \vec{\nabla} U, \vec{\nabla} U\rangle]^{\frac{1}{2}},$$

where the scalar product $\langle U, V\rangle$ is given by:

$$\langle U, V\rangle = \int_\Omega U(x,y)V(x,y)\, dx\, dy.$$

According to Theorem IV.1, convergence of the FEM on Ω is granted when h vanishes. In the case of non polygonal domain Ω, a more general result is provided in [19] to tackle the additional geometric truncation error. On the other hand, the constant C is not quantified in Theorem IV.1. In the FEM literature, more precise and specific estimation methods do exist to accurately quantify the discretization error (for instance, [20], [21]). In this section, our goal is slightly different: it is rather to propose qualitative and quantitative simulation results that illustrate the convergence of a FEM direct model in the context of EIT.

A. Discretization in the case of an explicit solution

A very simple way to estimate the discretization error is to use an example yielding an explicit analytic solution and to compare the latter with the numerical FEM simulation. Here, we study the example of a unit disk of uniform background conductivity $\sigma_0 = 1$, with a centered circular inhomogeneity σ of radius $R = 1/2$. The injected current distribution chosen is a sine function defined by

$$j(\theta) = \frac{d\bar{I}}{d\vec{t}} = \cos\theta,$$

where θ is the angle of the injection point in polar coordinate. The theoretical voltage boundary output expression is given in [22]:

$$\bar{V}^*(\theta) = \frac{1-\mu R^2}{1+\mu R^2}\cos\theta,$$

where

$$\mu = \frac{\sigma - 1}{\sigma + 1}.$$

Using CLCM again (*cf.* Fig. 4), we have focused on the difference between $\widehat{\bar{V}}$ and $\bar{V}^*$, w.r.t. σ on the one hand, and on the other hand w.r.t. the number of elements P. More precisely, the normalized distance

$$\nu(\sigma) := \frac{[\sum_{n=1}^{\bar{N}}(\bar{V}_n^* - \widehat{\bar{V}}_n)^2]^{\frac{1}{2}}}{[\sum_{n=1}^{\bar{N}}(\bar{V}_n^*)^2]^{\frac{1}{2}}},$$

has been computed, where $\bar{V}_n$ is the voltage value at the boundary node n.

Results are displayed on Fig. 5. First, one observes that the discretization error decreases (by a ratio of 3.5 by mesh-refinement step) along with the size of the largest element. When $\sigma = 1$, the conductivity distribution is uniform on Ω. Thus, the current paths are rectilinear (because of the 1-period sine current input) and there is no discretization error except the aforementioned truncation error that reveals negligible. Besides, the influence of $\ln \sigma$ is asymmetric w.r.t. $\sigma = 1$. Indeed, it can be checked that the curvature of current paths tends to be larger around the inhomogeneity domain when the latter is resistive ($\sigma < 1$), so the upper bound in eq. (14) is expected to increase accordingly. Hence, the piecewise linear paths yielded by the FEM on each element constitute a rougher approximation scheme. On the other hand, the striking similarity between the three curves is in accordance with the convergence rate of Theorem IV.1. For low contrasted conductivity distributions, the FEM reveals precise even with a limited number of elements. Furthermore, highly contrasted distributions do not require an ever increasing number of elements to keep the discretization error moderate, since the latter becomes nearly constant for $\sigma < 0.1$ and $\sigma > 3$, for any given number of elements. For intermediary mesh resolution ($P = 256$) and for conductive inhomogeneity ($\sigma > 1$), the FEM precision is about $\nu \approx 1.5\ 10^{-3}$. It corresponds to a $20 \log(\nu^{-1}) \approx 55$ dB *discretization signal-to-noise ratio* (D-SNR). For a finer mesh resolution ($P = 1024$), the D-SNR reaches 65 dB.

The latter study brings valuable information concerning the behavior of the discretization error in one particular case. From the qualitative point of view, it is expected that the same conclusions be available in a more general setting. This can be checked by resorting to the dual direct model.

B. Estimation of the discretization error based on the dual direct model

Equation (6) provides the direct model $(\bar{\boldsymbol{\imath}}, \boldsymbol{\sigma}) \rightarrow \bar{\boldsymbol{v}}$. However, one may notice that the 2D variational formulation (4) is symmetric in the sense that the substitutions $\sigma \rightarrow \sigma^{-1}$, $V \rightarrow -I$ and $I \rightarrow V$ leave eq. (4) unchanged. As studied in [23], [7], there also exists a

dual direct model $(\bar{\boldsymbol{v}}, \boldsymbol{\sigma}) \rightarrow \bar{\boldsymbol{\imath}}$, which reads [1]:

$$\bar{\boldsymbol{\imath}} = -\bar{\boldsymbol{P}} \boldsymbol{A}_{\boldsymbol{\sigma}^{-1}}^{-1} \bar{\boldsymbol{P}}^{\mathrm{t}} \boldsymbol{D} \bar{\boldsymbol{v}}. \tag{15}$$

The behaviour of the dual model can be deduced from that of the primal one by the simple substitution $\sigma \rightarrow \sigma^{-1}$. In particular, the dual model reveals more precise for resistive inhomogeneities $\sigma < 1$ in the explicit example Fig. 5.

To estimate the precision of the FEM model, we propose to combine the two available direct FEM models $(\bar{\boldsymbol{\imath}}, \boldsymbol{\sigma}) \rightarrow (\bar{\boldsymbol{v}}, \boldsymbol{\sigma}) \rightarrow (\bar{\boldsymbol{\imath}}', \boldsymbol{\sigma})$ and to compute the *boundary remainder* ρ defined by

$$\rho := \frac{\left\| \bar{\boldsymbol{\imath}}_0 - \bar{\boldsymbol{\imath}}_0' \right\|_2}{\left\| \bar{\boldsymbol{\imath}}_0 \right\|_2},$$

where $\bar{\boldsymbol{\imath}}_0$ is the centered value of $\bar{\boldsymbol{\imath}}$. According to Theorem IV.1, the boundary remainder tends to 0 when the mesh gets finer. This is attested by the values displayed on Fig. 7 for four different current distributions injected on the boundary of a CLCM (*cf.* Fig. 6).

Besides, using a uniform conductivity distribution (solid lines on Fig. 7), N being fixed, one can see that the accuracy of the direct model is better if the input current pattern is rather low-frequency. Moreover, current patterns with narrow spectra (*e.g.,* piecewise and half-period sine functions) yield comparatively faster convergence as N grows.

From a qualitative point of view, it is easy to guess that large variations in the input current pattern tend to create current paths that rewind to the boundary without entering deep into the medium. Moreover, such current paths may require a finer mesh to be correctly approximated according to Theorem IV.1, since the smaller values of their curvature radius correspond to larger values of $\max\left\{\left|\partial^2 V/\partial x^2\right|, \left|\partial^2 V/\partial x \partial y\right|, \left|\partial^2 V/\partial y^2\right|\right\}$.

It is also important to notice that the loss of accuracy in the case of a non uniform conductivity distribution (dashdotted line on Fig. 7) nearly corresponds to an upward shift of reduced amount compared to the potential influence of current pattern variations. Empirically, the rate of decrease of the *boundary remainder* ρ is almost equal to that of the normalized discretization error ν on Fig. 5, *i.e.,* about half a decade for $N \rightarrow 4N$ (remember the mathematical correspondance (9) between P and N). By linear regression

[1] Because eq. (3) is no longer valid in 3D, there is no such dual 3D formulation, to our best knowledge.

(in log-log scale), we obtain an approximate relation between $\nu(\sigma)$ and ρ :

$$\log \nu(\sigma) \approx \alpha \log \rho + \beta,$$

with $\alpha = 1.1378$, $\beta = -0.504$, with a relative error of 0.85% on $\log \nu$.

Extrapolation of this rule to other discretized domains provides a coarse but cheap estimator of the D-SNR. As an application, we have computed the resulting estimated D-SNR for various conductivity distributions displayed on the irregular domains of Fig. 8. The corresponding values are gathered in Table II, from which it can be seen that the estimated D-SNR ranges from 44 to 70 dB. Since the output round-off error is negligible, the resolution error of the direct problem reduces to the D-SNR.

In [24], the authors estimate that their real data have been obtained at a SNR of 66 dB (the corresponding measurement error is a part of the mathematical modeling error). In such a case, the FEM discretization error may represent another non negligible component of the total error. In [6], [7], [8], an inversion method has been proposed by the authors in the Bayesian framework. The different sources of errors have been considered as additive centered Gaussian white noises. The resulting method provides particularly robust and good reconstruction results from simulated data, even at a low SNR of 40 dB. Let us stress that such data have been obtained from a refined mesh, so that the discretization error is not artificially eliminated in the inversion step.

V. Conclusion

The goal of the present paper is to show that the finite element method (FEM) enables to build an accurate direct solver for electrical impedance tomography EIT.

First, we have studied the magnification of input round-off uncertainties through the FEM EIT direct model. We have derived an upper bound that involves the maximal contrast of the conductivity distribution and the condition number of the *uniform stiffness matrix* (USM). Examples of triangularized domains are provided (among which *concentric layer circular meshes*). Numerical computations of USM eigenvalues w.r.t. the number of nodes show that the magnification of round-off errors through the direct model is significant. However, for typical triangularized domains in EIT, it reveals small enough for

the direct model to be considered numerically stable. More generally, we have pointed out that the computation of the USM condition number is a suited tool to check whether a greater number of digits is required to encode the direct model.

In a second part, empirical evaluation of the discretization error has been performed by means of simulations. We have proposed an original method based on both primal and dual direct models to estimate the quality of convergence of the FEM solver. It has been raised that the smoothness of the input current pattern is an important factor to reduce the discretization error. Provided that the current patterns be smooth enough, one may easily obtain a signal-to-noise ratio of 50 dB w.r.t. numerical approximations, with a discrete mesh of about one thousand elements.

As a perspective, extension to 3D EIT direct models could be considered. Since 3D FEM models often involve a much larger number of nodes (tenths of thousands), avoiding instabilities should require to encode the data on a larger number of digits than provided by standard double precision. On the other hand, since the dual formulation (3) has no known counterpart in the 3D case, our study concerning the discretization error does not extend in a simple way.

Appendix

A. Proof of theorem III.1

The demonstration mainly consists in finding norms for involved matrices and in using the upper bound $\|\boldsymbol{M}\boldsymbol{u}\| \leqslant \|\boldsymbol{M}\|\,\|\boldsymbol{u}\|$, with $\|\boldsymbol{M}\| = \|\boldsymbol{M}\|_2 := \sqrt{r(\boldsymbol{M}^{\mathrm{t}}\boldsymbol{M})}$, where r stands for the spectral radius. From eq. (5) and (10), we obtain

$$\delta\boldsymbol{v} = (\boldsymbol{A}_{\boldsymbol{\sigma}+\delta\boldsymbol{\sigma}}^{-1} - \boldsymbol{A}_{\boldsymbol{\sigma}}^{-1})\boldsymbol{j} + \boldsymbol{A}_{\boldsymbol{\sigma}+\delta\boldsymbol{\sigma}}^{-1}\delta\boldsymbol{j} \tag{16}$$

and

$$\boldsymbol{A}_{\boldsymbol{\sigma}}\boldsymbol{v} = \boldsymbol{j}, \tag{17}$$

which are respectively useful to find an upper bound for $\|\delta\boldsymbol{v}\|$ and a lower bound for $\|\boldsymbol{v}\|$.

From eq. (8), it appears that $\boldsymbol{A}_{\boldsymbol{\sigma}}$ is positive definite. Hence, we get

$$\|\boldsymbol{A}_{\boldsymbol{\sigma}}\| := \sup_{\|\boldsymbol{v}\|=1} \boldsymbol{v}^{\mathrm{t}}\boldsymbol{A}_{\boldsymbol{\sigma}}\boldsymbol{v} = \lambda_{\boldsymbol{A}_{\boldsymbol{\sigma}}}^{\max}$$

and

$$\left\|\boldsymbol{A}_{\boldsymbol{\sigma}}^{-1}\right\|^{-1} := \inf_{\|\boldsymbol{v}\|=1} \boldsymbol{v}^{\mathrm{t}}\boldsymbol{A}_{\boldsymbol{\sigma}}\boldsymbol{v} = \lambda_{\boldsymbol{A}_{\boldsymbol{\sigma}}}^{\min},$$

respectively for the smallest and the largest eigenvalue of $\boldsymbol{A}_{\boldsymbol{\sigma}}$. Since $\boldsymbol{Q}$ is a full rank matrix and $\boldsymbol{\Theta} = \boldsymbol{Q}^{\mathrm{t}}\boldsymbol{Q}$ is Hermitian, we have

$$\forall\ \boldsymbol{v} \text{ s.t. } \|\boldsymbol{v}\| = 1,\ \lambda_{\boldsymbol{\Theta}}^{\min} \leqslant \|\boldsymbol{Q}\boldsymbol{v}\|^2 \leqslant \lambda_{\boldsymbol{\Theta}}^{\max}. \tag{18}$$

Furthermore, since $\boldsymbol{\Delta}_{\boldsymbol{\sigma}}$ is a diagonal positive definite matrix with components of $\boldsymbol{\sigma}$ on its diagonal, we have

$$\forall\ \boldsymbol{u} \text{ s.t. } \|\boldsymbol{u}\| = 1,\ \left\|\boldsymbol{\Delta}_{\boldsymbol{\sigma}}^{-1}\right\|^{-1} \leqslant \boldsymbol{u}^{\mathrm{t}}\boldsymbol{\Delta}_{\boldsymbol{\sigma}}\boldsymbol{u} \leqslant \|\boldsymbol{\Delta}_{\boldsymbol{\sigma}}\|.$$

Taking $\boldsymbol{u} = \boldsymbol{Q}\boldsymbol{v}/\|\boldsymbol{Q}\boldsymbol{v}\|$, we obtain:

$$\forall\ \boldsymbol{v} \text{ s.t. } \|\boldsymbol{v}\| = 1,\ \boldsymbol{\sigma}_{\min} = \left\|\boldsymbol{\Delta}_{\boldsymbol{\sigma}}^{-\frac{1}{2}}\right\|^{-2} \leqslant \frac{\left\|\boldsymbol{\Delta}_{\boldsymbol{\sigma}}^{\frac{1}{2}}\boldsymbol{Q}\boldsymbol{v}\right\|^2}{\|\boldsymbol{Q}\boldsymbol{v}\|^2} \leqslant \left\|\boldsymbol{\Delta}_{\boldsymbol{\sigma}}^{\frac{1}{2}}\right\|^2 = \boldsymbol{\sigma}_{\max}. \tag{19}$$

Since we have $\boldsymbol{v}^{\mathrm{t}}\boldsymbol{A}_{\boldsymbol{\sigma}}\boldsymbol{v} = \left\|\boldsymbol{\Delta}_{\boldsymbol{\sigma}}^{\frac{1}{2}}\boldsymbol{Q}\boldsymbol{v}\right\|^2$, multiplying eq. (18) by eq. (19) yields:

$$\boldsymbol{\sigma}_{\min}\lambda_{\boldsymbol{\Theta}}^{\min} \leqslant \|\boldsymbol{\Delta}_{\boldsymbol{\sigma}}\boldsymbol{Q}\boldsymbol{v}\|^2 \leqslant \boldsymbol{\sigma}_{\max}\lambda_{\boldsymbol{\Theta}}^{\max},$$

which is equivalent to

$$\forall\ \boldsymbol{v} \text{ s.t. } \|\boldsymbol{v}\| = 1,\ \boldsymbol{\sigma}_{\min}\lambda_{\boldsymbol{\Theta}}^{\min} \leqslant \left\|\boldsymbol{A}_{\boldsymbol{\sigma}}^{-1}\right\|^{-1} \leqslant \boldsymbol{v}^{\mathrm{t}}\boldsymbol{A}_{\boldsymbol{\sigma}}\boldsymbol{v} \leqslant \|\boldsymbol{A}_{\boldsymbol{\sigma}}\| \leqslant \boldsymbol{\sigma}_{\max}\lambda_{\boldsymbol{\Theta}}^{\max}. \tag{20}$$

Eq. (11) yields

$$|\delta\boldsymbol{\sigma}|_{\max} < \boldsymbol{\sigma}_{\min}.$$

Thus, from eq. (20), we obtain

$$\left\|\boldsymbol{A}_{\boldsymbol{\sigma}+\delta\boldsymbol{\sigma}}^{-1}\right\| \leqslant \frac{1}{(\boldsymbol{\sigma}+\delta\boldsymbol{\sigma})_{\min}\lambda_{\boldsymbol{\Theta}}^{\min}} \leqslant \frac{1}{(\boldsymbol{\sigma}_{\min} - |\delta\boldsymbol{\sigma}|_{\max})\lambda_{\boldsymbol{\Theta}}^{\min}} \tag{21}$$

for the upper bounding of $\|\delta\boldsymbol{v}\|$ and

$$\|\boldsymbol{A}_{\boldsymbol{\sigma}}\| \leqslant \boldsymbol{\sigma}_{\max}\lambda_{\boldsymbol{\Theta}}^{\max} \tag{22}$$

for the lower bounding of $\|\boldsymbol{v}\|$. From eq. (17), the latter is straightforward:

$$\|\boldsymbol{v}\|^{-1} \leqslant \boldsymbol{\sigma}_{\max}\lambda_{\boldsymbol{\Theta}}^{\max}\|\boldsymbol{j}\|^{-1}. \tag{23}$$

There remains to find an upper bound for $\left\|\boldsymbol{A}_{\boldsymbol{\sigma}+\delta\boldsymbol{\sigma}}^{-1}-\boldsymbol{A}_{\boldsymbol{\sigma}}^{-1}\right\|$. For this, we use the following lemma.

Lemma A.1 (Perturbation theory on matrices) If the invertible matrix $\boldsymbol{M}$ is perturbed by a matrix $\delta\boldsymbol{M}$, and if $\left\|\boldsymbol{M}^{-1}\right\|\|\delta\boldsymbol{M}\|<1$, then the norm of the perturbation $\delta(\boldsymbol{M}^{-1}):=(\boldsymbol{M}+\delta\boldsymbol{M})^{-1}-\boldsymbol{M}^{-1}$ on the inverse $\boldsymbol{M}^{-1}$ is bounded by:

$$\left\|\delta(\boldsymbol{M}^{-1})\right\|\leqslant\frac{\left\|\boldsymbol{M}^{-1}\right\|^2\|\delta\boldsymbol{M}\|}{1-\left\|\boldsymbol{M}^{-1}\right\|\|\delta\boldsymbol{M}\|}. \tag{24}$$

A demonstration of this result can be found in [25]. As a direct application, consider $\boldsymbol{M}=\boldsymbol{A}_{\boldsymbol{\sigma}}$ and $\delta\boldsymbol{M}=\boldsymbol{A}_{\delta\boldsymbol{\sigma}}$. Indeed, $\boldsymbol{A}_{\boldsymbol{\sigma}}$ being linear w.r.t. $\boldsymbol{\sigma}$, we have:

$$\boldsymbol{A}_{\boldsymbol{\sigma}+\delta\boldsymbol{\sigma}}=\boldsymbol{A}_{\boldsymbol{\sigma}}+\boldsymbol{A}_{\delta\boldsymbol{\sigma}}.$$

Besides, according to eq. (8), we have

$$\boldsymbol{A}_{\delta\boldsymbol{\sigma}}=\boldsymbol{Q}^{\mathrm{t}}\boldsymbol{\Delta}_{\delta\boldsymbol{\sigma}}\boldsymbol{Q}$$

so that

$$\|\boldsymbol{A}_{\delta\boldsymbol{\sigma}}\|\leqslant\left\|\boldsymbol{Q}^{\mathrm{t}}\boldsymbol{Q}\right\|\|\boldsymbol{\Delta}_{\delta\boldsymbol{\sigma}}\|.$$

Since $\|\boldsymbol{\Delta}_{\delta\boldsymbol{\sigma}}\|=\|\delta\boldsymbol{\sigma}\|_\infty=|\delta\boldsymbol{\sigma}|_{\max}$, $\left\|\boldsymbol{Q}^{\mathrm{t}}\boldsymbol{Q}\right\|=\lambda_{\boldsymbol{\Theta}}^{\max}$, and (from eq. (20))

$$\left\|\boldsymbol{A}_{\boldsymbol{\sigma}}^{-1}\right\|\leqslant\frac{1}{\boldsymbol{\sigma}_{\min}\lambda_{\boldsymbol{\Theta}}^{\min}},$$

the sufficient condition $\left\|\boldsymbol{M}^{-1}\right\|\|\delta\boldsymbol{M}\|<1$ is checked if $|\delta\boldsymbol{\sigma}|_{\max}<\boldsymbol{\sigma}_{\min}\lambda_{\boldsymbol{\Theta}}^{\min}/\lambda_{\boldsymbol{\Theta}}^{\max}$, which does correspond to condition (11) in the theorem. Consequently,

$$\left\|\boldsymbol{A}_{\boldsymbol{\sigma}+\delta\boldsymbol{\sigma}}^{-1}-\boldsymbol{A}_{\boldsymbol{\sigma}}^{-1}\right\|\leqslant\frac{\lambda_{\boldsymbol{\Theta}}^{\max}|\delta\boldsymbol{\sigma}|_{\max}}{\boldsymbol{\sigma}_{\min}\lambda_{\boldsymbol{\Theta}}^{\min}(\boldsymbol{\sigma}_{\min}\lambda_{\boldsymbol{\Theta}}^{\min}-|\delta\boldsymbol{\sigma}|_{\max}\lambda_{\boldsymbol{\Theta}}^{\max})}. \tag{25}$$

Finally, eq. (21) and (25) yield the expected bounds. Given eq. (16), we obtain

$$\|\delta\bar{\boldsymbol{v}}\|\leqslant\frac{\lambda_{\boldsymbol{\Theta}}^{\max}|\delta\boldsymbol{\sigma}|_{\max}}{\boldsymbol{\sigma}_{\min}\lambda_{\boldsymbol{\Theta}}^{\min}(\boldsymbol{\sigma}_{\min}\lambda_{\boldsymbol{\Theta}}^{\min}-|\delta\boldsymbol{\sigma}|_{\max}\lambda_{\boldsymbol{\Theta}}^{\max})}\|\boldsymbol{j}\|+\frac{\|\delta\boldsymbol{j}\|}{(\boldsymbol{\sigma}_{\min}-|\delta\boldsymbol{\sigma}|_{\max})\lambda_{\boldsymbol{\Theta}}^{\min}}. \tag{26}$$

From (23) and (26), we finally get

$$\frac{\|\delta\boldsymbol{v}\|}{\|\boldsymbol{v}\|}\leqslant\frac{\boldsymbol{\sigma}_{\max}\lambda_{\boldsymbol{\Theta}}^{\max 2}|\delta\boldsymbol{\sigma}|_{\max}}{\boldsymbol{\sigma}_{\min}\lambda_{\boldsymbol{\Theta}}^{\min}(\boldsymbol{\sigma}_{\min}\lambda_{\boldsymbol{\Theta}}^{\min}-|\delta\boldsymbol{\sigma}|_{\max}\lambda_{\boldsymbol{\Theta}}^{\max})}+\frac{\boldsymbol{\sigma}_{\max}\lambda_{\boldsymbol{\Theta}}^{\max}\|\delta\boldsymbol{j}\|}{(\boldsymbol{\sigma}_{\min}-|\delta\boldsymbol{\sigma}|_{\max})\lambda_{\boldsymbol{\Theta}}^{\min}\|\boldsymbol{j}\|},$$

which is the announced result. □

References

[1] M. Tasto and H. Schomberg, "Object reconstruction from projections and some non-linear extensions", *Pattern Recognition and Signal Processing (ed. C. H. Chen)*, pp. 485–503, 1978.

[2] L. R. Price, "Electrical impedance computed tomography (ICT): a new CT Technique", *IEEE Transactions on Nuclear Sciences*, vol. 26, no. 2, pp. 2736–2739, April 1979.

[3] K. Dines and R. Lytle, "Analysis of electrical imaging", *Geophysics*, vol. 46, no. 7, pp. 1025–1036, July 1981.

[4] H. Kardestuncer, D. H. Norrie, and F. Brezzi, *Finite Element Handbook*, McGraw-Hill Book Company, 1987.

[5] G. Strang and G. Fix, *An analysis of the finite element method*, Prentice-Hall, 1973.

[6] T. Martin and J. Idier, "A FEM-based nonlinear MAP estimator in electrical impedance tomography", in *Proceedings of the International Conference on Image Processing*, Santa Barbara, USA, October 1997, pp. 684–687.

[7] T. Martin, *Inversion bayésienne du problème non linéaire de tomographie d'impédance électrique modélisé par une méthode d'éléments finis*, PhD thesis, Université de Paris-Sud, Orsay, novembre 1997.

[8] T. Martin and J. Idier, "Estimating a conductivity distribution via a FEM-based nonlinear Bayesian method", *European Physical Journal, Applied Physics*, vol. 1, pp. 87–91, January 1998.

[9] T. Murai and Y. Kagawa, "Electrical impedance computed tomography based on a finite element model", *IEEE Transactions on Biomedical Engineering*, vol. 32, no. 3, pp. 177–184, March 1985.

[10] T. Yorkey, G. Webster, and W. Tompkins, "Comparing reconstruction algorithms for electrical impedance tomography", *IEEE Transactions on Biomedical Engineering*, pp. 843–852, 1987.

[11] J. Webster, *Electrical Impedance Tomography*, Adam Hilger, IOP Publishing Ltd, 1990.

[12] E. J. Woo, P. Hua, J. G. Webster, and W. J. Tompkins, "Measuring lung resistivity using electrical impedance tomography", *IEEE Transactions on Biomedical Engineering*, vol. 39, no. 7, pp. 756–760, July 1992.

[13] A. J. Davies, *The Finite Element Method: A First Approach*, Oxford Applied Mathematics and Computing Science Series, 1980.

[14] W. Press, S. Teukolsky, W. Vetterling, and B. Flannery, *Numerical recipes in C, the art of scientific computing, second edition*, Cambridge Univ. Press, New York, 1992.

[15] H. Jain, D. Isaacson, P. M. Edic, and J. C. Newell, "Electrical impedance tomography of complex conductivity distributions with noncircular boundary", *IEEE Transactions on Biomedical Engineering*, vol. 44, no. 11, pp. 1051–1060, November 1997.

[16] F. X. Zgainski, Y. Maréchal, J. Coulomb, and P. Thomas, "Un critère de qualité généraliste *a priori* pour le maillage dans la méthode des éléments finis", in *Numélec'97 : seconde conférence européenne sur les méthodes numériques en électromagnétisme*, Lyon, mars 1997, pp. 100–101.

[17] P. L. George, *Automatic Mesh Generation: Application to Finite Element Methods*, John Wiley & Sons, 1991.

[18] T. Martin and J. Idier, "A Bayesian non-linear inverse approach for electrical impedance tomography", in *2nd Intern. Conf. Inverse Problems in Engng.*, Le Croisic, France, June 1996, pp. 473–480.

[19] P. Raviart and J. Thomas, *Introduction à l'analyse numérique des équations aux dérivées partielles*, Masson, 1988.

[20] I. Babuska and W. Rheinboldt, "Error estimates for adaptive finite element computations", *SIAM Journal of Numerical Analysis*, vol. 15, no. 4, pp. 736–754, August 1978.

[21] I. Babuska and W. Rheinboldt, "On the reliability and optimality of the finite element method", *Comput. Struct.*, vol. 10, pp. 87–94, 1979.

[22] D. Isaacson, "Distinguishability of conductivities by electric current computed tomography", *IEEE Transactions on Medical Imaging*, vol. 5, no. 2, pp. 91–95, June 1986.

[23] R. V. Kohn and A. McKenney, "Numerical implementation of a variational method for electrical impedance tomography", *Inverse Problems*, pp. 389–414, 1990.

[24] P. Hua, E. Woo, J. Webster, and W. Tompkins, "Iterative reconstruction methods using regularization and optimal current patterns in electrical impedance tomography.", *IEEE Transactions on Medical Imaging*, pp. 621–628, December 1991.

[25] J. Wilkinson, *The algebraic eigenvalue problem*, Clarendon Press, Oxford, 1965.

Tables

TABLE I USM $\boldsymbol{\Theta}$ eigenvalues and accuracy of the output coding for the meshes of 8 and 4. The contrast is $\rho_\sigma = 100$ and the numbers are coded on 16 digits, yielding $\epsilon = 2.22\ 10^{-16}$ as floating point relative uncertainty. The range of $\|\delta\bar{\boldsymbol{u}}\|_2^{\sup}$ provides an output accuracy greater than 6 digits.

TABLE II Values of the remainder and of the estimated D-SNR ($= -20 \log \nu$) for the discretized domain of Fig. 8 a,b,c & d for uniform and non uniform distribution. The current distribution chosen is the piecewise sine distribution displayed Fig. 6 b. For comparison, two points of the CLCM case (*cf.* Fig. 4, $\sigma = 10$) are displayed here. All the D-SNR are above 40 dB.

Figures

Fig. 1 Exemple of CLCM with 8 layers (N=145, P=256). The black points on Fig. b locate the 4.5% nonzero elements in the resulting $\boldsymbol{A_\sigma}$ stiffness matrix.

Fig. 2 Solid line ($-$): computational cost of the resolution of the linear system (5) w.r.t. the number of nodes N for CLCM meshes; dashdotted line ($-\cdot$): computational cost of the multiplication of a full matrix ($N \times N$) by a vector, for sake of comparison. If N is above 100, which is rather small for FEM EIT models, solving the direct problem is cheaper than a full matrix multiplication of same size.

Fig. 3 Behavior of the extreme eigenvalues of the USM$\boldsymbol{\Theta}$ w.r.t. the number of nodes N with the CLCM family, in a log-log scale. ($-$) $\lambda_{\boldsymbol{\Theta}}^{\max}$, ($-\cdot$) $\lambda_{\boldsymbol{\Theta}}^{\min}$.

Fig. 4 Two examples of CLCM with a centered circular inhomogeneity.

Fig. 5 Study of the discretization error $\nu(\sigma)$ for a circular domain with a circular inhomogeneity of conductivity σ. P is the number of mesh elements. $\nu(\sigma)$ decreases when the mesh gets finer, in an asymmetrical way w.r.t. the vertical asymptote $\sigma = 1$.

Fig. 6 Four different boudary current patterns $\bar{\boldsymbol{\imath}}$ used to compute the boundary remainder ρ, as displayed on Fig. 7 with the corresponding marks $+, \circ, \times$ and $*$.

Fig. 7 Behavior of the remainder as a function of the number of nodes N for the current distributions of Fig. 6 on CLCM. ($-$) uniform conductivity distribution, ($-\cdot$) distribution

with a centered circular inhomogeneity $\sigma = 10$ (Fig. 4).

Fig. 8 Two refinement scales are chosen for the discretization of a peanut-shaped domain (above) and a potato-shaped domain (below). For each of theses domains, the remainder ρ is computed from an inhomogeneous conductivity distribution.

Domain	a	b	c	d	CLCM	CLCM
# nodes N	174	552	184	639	145	545
$\lambda_{\mathbf{\Theta}}^{\max}$	8.426	10.386	6.378	7.03	7.06	7.79
$\lambda_{\mathbf{\Theta}}^{\min}$	0.0241	0.0077	0.0040	0.0010	0.0121	0.00294
$\|\delta\bar{\boldsymbol{u}}\|_2^{\sup}$	$2.72\ 10^{-9}$	$4.04\ 10^{-8}$	$5.65\ 10^{-8}$	$1.10\ 10^{-6}$	$7.57\ 10^{-9}$	$1.56\ 10^{-7}$

TABLE I

USM $\mathbf{\Theta}$ EIGENVALUES AND ACCURACY OF THE OUTPUT CODING FOR THE MESHES OF 8 AND 4. THE CONTRAST IS $\rho_\sigma = 100$ AND THE NUMBERS ARE CODED ON 16 DIGITS, YIELDING $\epsilon = 2.22\ 10^{-16}$ AS FLOATING POINT RELATIVE UNCERTAINTY. THE RANGE OF $\|\delta\bar{\boldsymbol{u}}\|_2^{\sup}$ PROVIDES AN OUTPUT ACCURACY GREATER THAN 6 DIGITS.

Distribution		a	b	c	d	CLCM	CLCM
# elements P		296	1002	336	1217	256	1024
σ unif.	ρ	$6.90\ 10^{-3}$	$2.86\ 10^{-3}$	$2.84\ 10^{-3}$	$1.70\ 10^{-3}$	$9.97\ 10^{-3}$	$2.57\ 10^{-3}$
	D-SNR	60 dB	68 dB	68 dB	73 dB	56 dB	69 dB
σ inhom.	ρ	$3.47\ 10^{-2}$	$1.43\ 10^{-2}$	$3.15\ 10^{-2}$	$1.29\ 10^{-2}$	$1.27\ 10^{-2}$	$5.275\ 10^{-3}$
	D-SNR	44 dB	52 dB	45 dB	54 dB	54 dB	62 dB

TABLE II

VALUES OF THE REMAINDER AND OF THE ESTIMATED D-SNR ($= -20 \log \nu$) FOR THE DISCRETIZED DOMAIN OF FIG. 8 A,B,C & D FOR UNIFORM AND NON UNIFORM DISTRIBUTION. THE CURRENT DISTRIBUTION CHOSEN IS THE PIECEWISE SINE DISTRIBUTION DISPLAYED FIG. 6 B. FOR COMPARISON, TWO POINTS OF THE CLCM CASE (*cf.* FIG. 4, $\sigma = 10$) ARE DISPLAYED HERE. ALL THE D-SNR ARE ABOVE 40 DB.

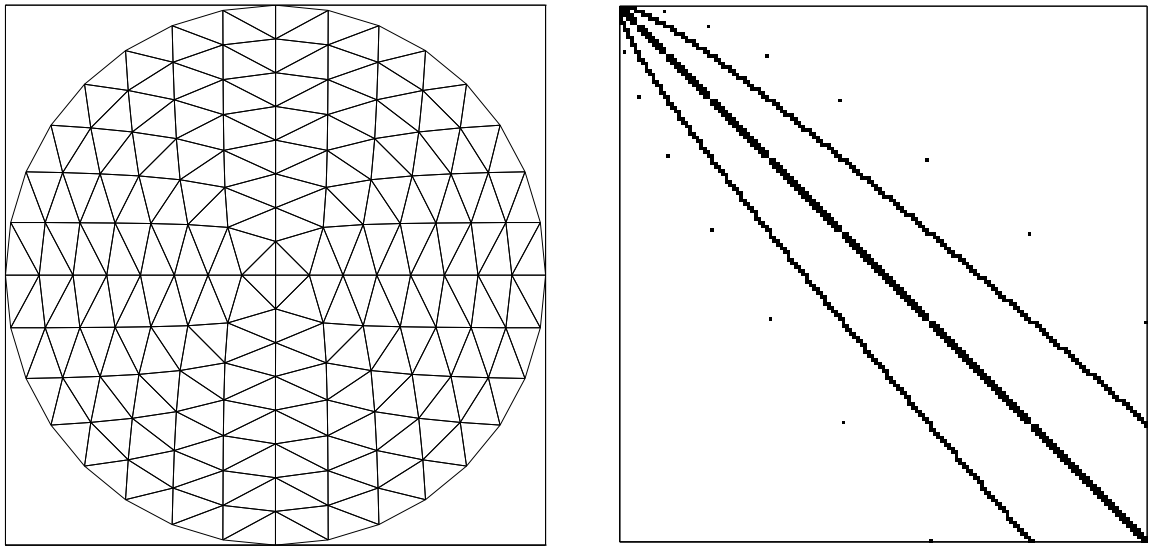

a - CLCM with 8 layers b - Corresponding sparsity of $\boldsymbol{A}_{\boldsymbol{\sigma}}$

Fig. 1. Exemple of CLCM with 8 layers (N=145, P=256). The black points on Fig. b locate the 4.5% nonzero elements in the resulting $\boldsymbol{A}_{\boldsymbol{\sigma}}$ stiffness matrix.

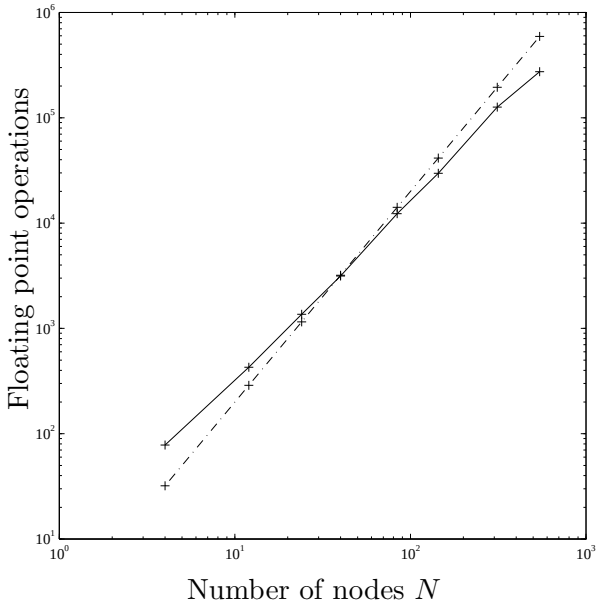

Fig. 2. Solid line (−): computational cost of the resolution of the linear system (5) w.r.t. the number of nodes N for CLCM meshes; dashdotted line (−·): computational cost of the multiplication of a full matrix ($N \times N$) by a vector, for sake of comparison. If N is above 100, which is rather small for FEM EIT models, solving the direct problem is cheaper than a full matrix multiplication of same size.

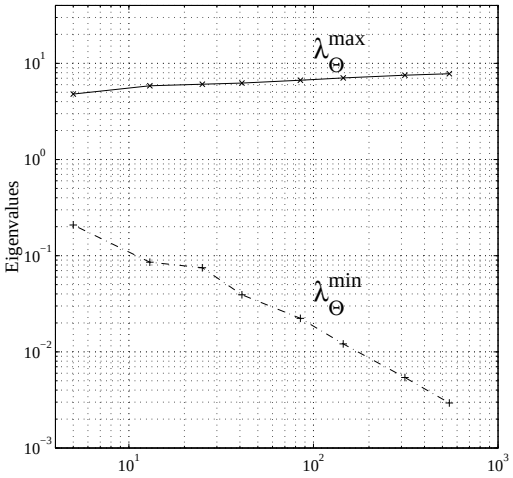

Fig. 3. Behavior of the extreme eigenvalues of the USM $\mathbf{\Theta}$ w.r.t. the number of nodes N with the CLCM family, in a log-log scale. $(-)$ $\lambda_{\mathbf{\Theta}}^{\max}$, $(-\cdot)$ $\lambda_{\mathbf{\Theta}}^{\min}$.

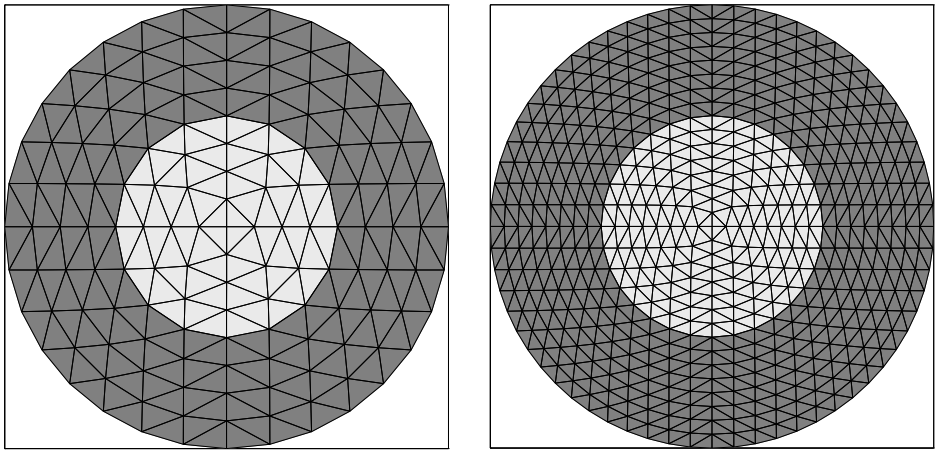

$P = 256, N = 145$ $P = 1024, N = 545$

Fig. 4. Two examples of CLCM with a centered circular inhomogeneity.

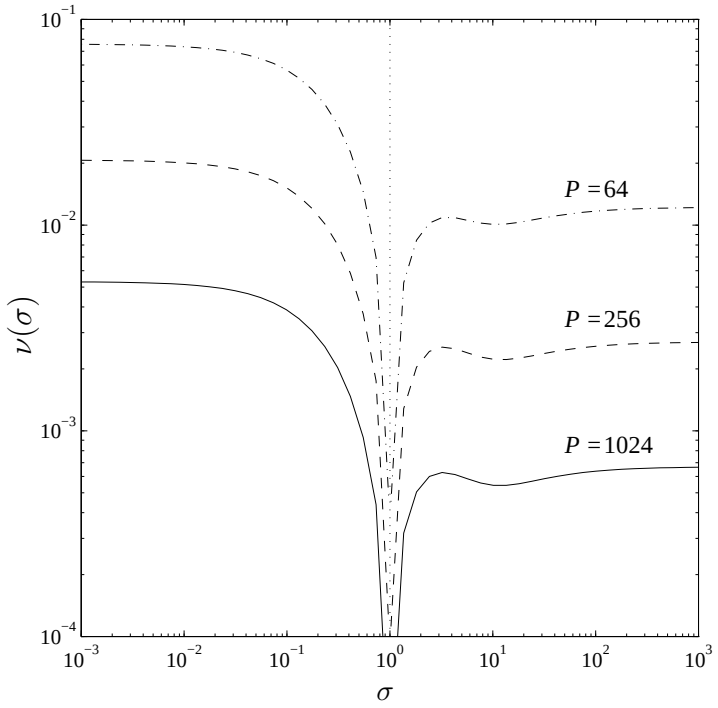

Fig. 5. Study of the discretization error $\nu(\sigma)$ for a circular domain with a circular inhomogeneity of conductivity σ. P is the number of mesh elements. $\nu(\sigma)$ decreases when the mesh gets finer, in an asymmetrical way w.r.t. the vertical asymptote $\sigma = 1$.

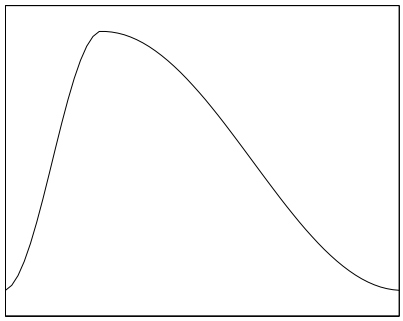

(+) piecewise sine function.

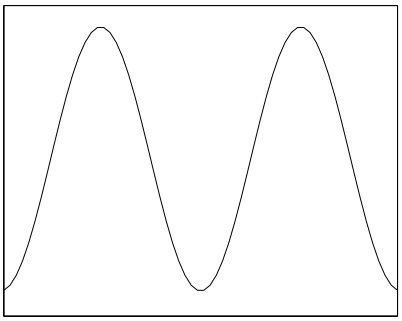

(∘) Half-period sine distribution.

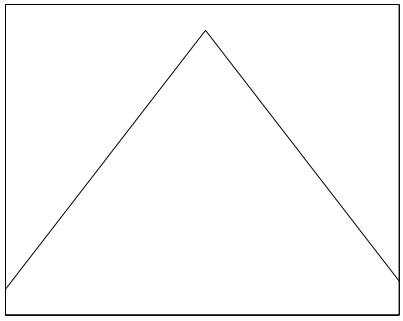

(×) Basic triangle function.

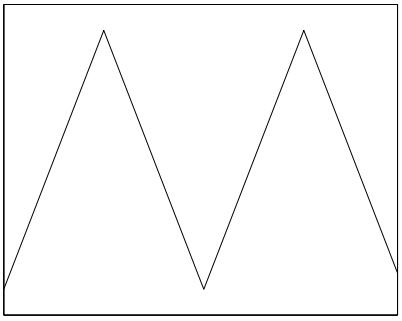

(∗) Half-period triangle function.

Fig. 6. Four different boudary current patterns $\bar{\boldsymbol{\imath}}$ used to compute the boundary remainder ρ, as displayed on Fig. 7 with the corresponding marks $+, \circ, \times$ and $*$.

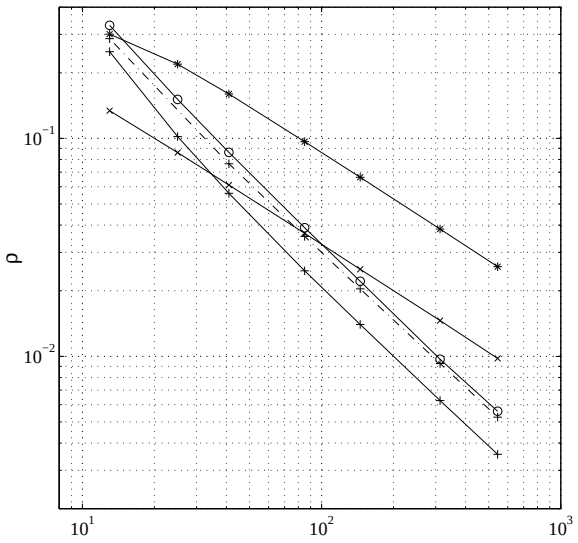

Fig. 7. Behavior of the remainder as a function of the number of nodes N for the current distributions of Fig. 6 on CLCM. $(-)$ uniform conductivity distribution, $(-\cdot)$ distribution with a centered circular inhomogeneity $\sigma = 10$ (Fig. 4).

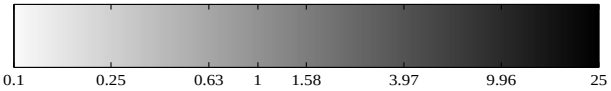

Logarithmic scale for the conductivity distributions.

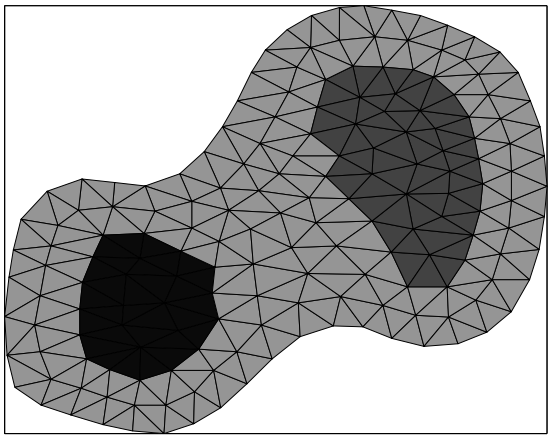

a - Medium discretization, 2 inhomoneous areas.

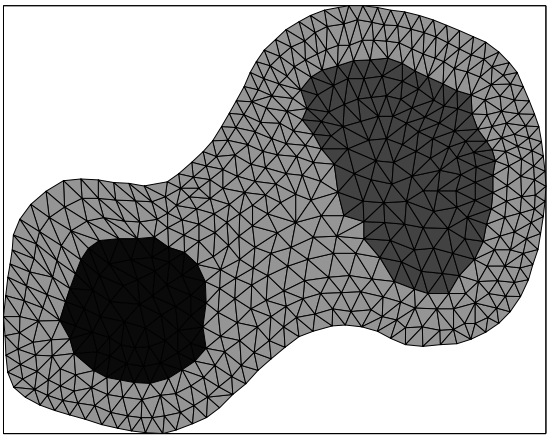

b - Fine discretization, 2 inhomoneous areas.

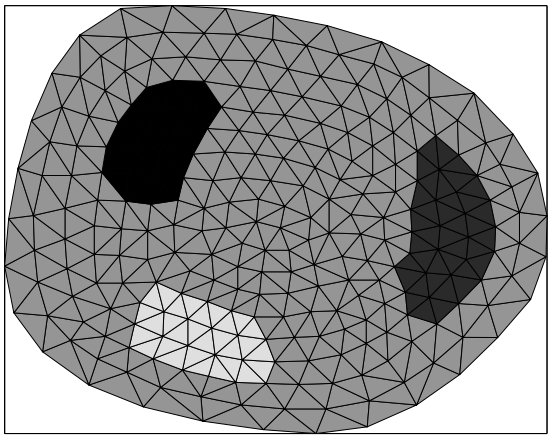

c - Medium discretization, 3 inhomogeneous areas.

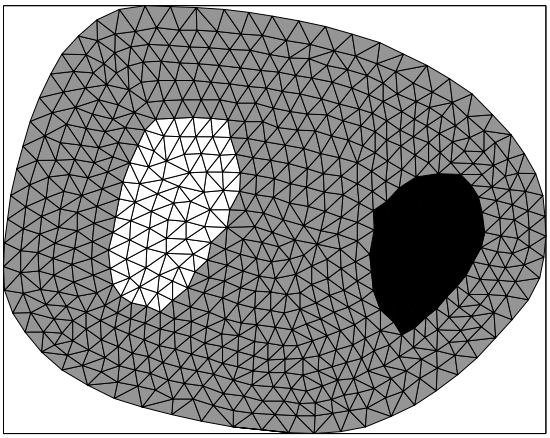

d - Fine discretization, 2 inhomoneous areas.

Fig. 8. Two refinement scales are chosen for the discretization of a peanut-shaped domain (above) and a potato-shaped domain (below). For each of theses domains, the remainder ρ is computed from an inhomogeneous conductivity distribution.